Computational and dark-field ghost imaging with ultraviolet light

Jiaqi Song,[1] Baolei Liu,[1,*] Yao Wang,[1] Chaohao Chen,[2] Xuchen Shan,[1] Xiaolan Zhong,[1,4] Ling-An Wu,[3] and Fan Wang[1]

[1]*School of Physics, Beihang University, Beijing 102206, China*
[2]*Australian Research Council Centre of Excellence for Transformative Meta-Optical Systems, Department of Electronic Materials Engineering, Research School of Physics, The Australian National University, Canberra, ACT 2600, Australia*
[3]*Institute of Physics, Chinese Academy of Sciences, Beijing 100190, China*
[4]*e-mail: zhongxl@buaa.edu.cn*
Corresponding author: liubaolei@buaa.edu.cn

Ultraviolet (UV) imaging enables a diverse array of applications, such as material composition analysis, biological fluorescence imaging, and detecting defects in semiconductor manufacturing. However, scientific-grade UV cameras with high quantum efficiency are expensive and include complex thermoelectric cooling systems. Here, we demonstrate a UV computational ghost imaging (UV-CGI) method to provide a cost-effective UV imaging and detection strategy. By applying spatial–temporal illumination patterns and using a 325 nm laser source, a single-pixel detector is enough to reconstruct the images of objects. We use UV-CGI to distinguish four UV-sensitive sunscreen areas with different densities on a sample. Furthermore, we demonstrate dark-field UV-CGI in both transmission and reflection schemes. By only collecting the scattered light from objects, we can detect the edges of pure phase objects and small scratches on a compact disc. Our results showcase a feasible low-cost solution for nondestructive UV imaging and detection. By combining it with other imaging techniques, such as hyperspectral imaging or time-resolved imaging, a compact and versatile UV computational imaging platform may be realized for future applications.   © 2024 Chinese Laser Press

https://doi.org/10.1364/PRJ.503974

1. INTRODUCTION

Ghost imaging (GI), an alternative imaging technique that uses only a single-pixel detector (SPD), has been widely studied in both quantum and classical optics [1,2]. Traditional GI uses a beam splitter to divide random light fields into two light paths [3]; one path uses an arrayed detector to record the spatial distribution of the random light field, and the other uses an SPD to collect the intensity of the transmitted or reflected light from an object in that beam. The object's image can be reconstructed via the second-order correlation function between the measurements of these two detectors. Computational ghost imaging (CGI), as a modification of GI, removes the need for the arrayed detection of the light field by adopting a spatial light modulator (SLM) to generate a sequence of programmable patterns to illuminate the object [4,5]. This is closely related to the scheme of single-pixel cameras, which use the SLM to modulate the field at the image plane and an SPD to measure the light intensities after the modulation [6,7]. One advantage of GI/CGI is that it can obtain an image with many fewer measurements than the total number of image pixels, a strategy also

known as compressive sampling or subsampling [6,8]. Due to its easy implementation, GI/CGI has been extended into various applications, such as LiDAR [9,10], cytometry [11], hyperspectral imaging [12–14], and phase imaging [15,16]. Another advantage of GI/CGI is that it can be achieved with a wide range of electromagnetic waves since different kinds of spatial modulators can be used, for example, rotating ground-glass diffusers [9,17–19], liquid crystal SLMs [20], digital micromirror devices (DMDs) [21–23], or coded masks [24,25]. To date, GI/CGI has been realized with entangled photon pairs [1,26], visible light [27,28], near-infrared [29], mid-infrared [30], and terahertz wavelengths [20,31,32], X-rays [33–36], atoms [37], electrons [38], and neutrons [39,40]. However, GI/CGI has rarely been studied in the ultraviolet (UV) band. Recently, single-pixel cameras in the UV band were employed to capture flame chemiluminescence [25,41] and identify different transparent objects with a single-photon avalanche diode [42]. Many UV-sensitive applications with active illumination need to be further studied.

Generally, UV imaging can be divided into two types: UV-fluorescence imaging and UV-reflectance imaging. In the

former, objects absorb UV light and emit fluorescence of longer wavelengths, such as real-time nondestructive monitoring of food freshness [43]. In the latter, a UV camera is used to collect the light reflected from the objects. UV reflectance imaging can detect hidden damages that are not sensitive to visible light/human eyes [44,45]. Due to its short wavelength, UV light is more easily scattered by smaller features that are not obvious at longer wavelengths [46,47]. However, high-performance UV cameras are expensive, which limits their usage in practical applications.

In this study, we report the applications of UV-CGI in dark-field imaging as well as imaging of substances with different densities under ordinary conditions. First, we used samples containing UV-sensitive sunscreen. Second, a sample was formed by dispersing different amounts of sunscreen on a piece of paper so that the different grayscale values of the reconstructed image revealed the different amounts of sunscreen. The lower the grayscale value, the higher the density of sunscreen due to the higher absorption under UV light irradiation. Furthermore, we propose dark-field UV-CGI for detecting phase objects and slight damages on a compact disc (CD). By only detecting the scattered light from the samples, we can retrieve the edges of the phase objects and images of the defects. Our technique broadens the application possibilities of CGI in the UV range and provides a scalable low-cost UV imaging method, which can be further combined with hyperspectral and time-resolved imaging and be integrated into miniature optical systems.

2. THEORY

A. Principles of Ghost Imaging

In GI, an object $O(x_0, y_0)$ is illuminated sequentially by N illumination patterns P, so that the intensities I of the corresponding total reflected or transmitted light, measured by an SPD, can be expressed as

$$I_i = \int P_i(x_0, y_0) \cdot O(x_0, y_0) dx_0 dy_0, \quad (1)$$

where $i = 1, 2, \ldots, N$ is the index of the pattern, and x_0 and y_0 are spatial coordinates. To retrieve the image, a traditional correlation algorithm can be used, such as [5]

$$O(x_0, y_0) = \langle IP(x_0, y_0) \rangle - \langle I \rangle \langle P(x_0, y_0) \rangle, \quad (2)$$

where $\langle \ldots \rangle$ is the ensemble average over the distribution of the patterns. By applying compressive sensing algorithms, high-quality images can be retrieved with a low sampling ratio.

B. Principles of Dark-Field UV-CGI

We further develop dark-field UV-CGI that has advantages in imaging phase objects and small scattering features such as scratches on a CD. Compared with traditional GI/CGI, dark-field CGI only collects the scattered light from objects [19], instead of the total intensity I_i, by using a beam stop to block the directly reflected/transmitted light (the detailed experimental setup is presented in Figs. 4 and 5 and the following section). After the pattern illuminates the object, the total electric field amplitude E_{total} at the object plane can be briefly expressed as follows:

$$E_{total}(x_0, y_0) = E_r(x_0, y_0) + E_t(x_0, y_0) + E_s(x_0, y_0), \quad (3)$$

where $E_r(x_0, y_0) = O_r(x_0, y_0) \cdot E_i(x_0, y_0)$ is the reflected wave, $E_t(x_0, y_0) = O_t(x_0, y_0) \cdot E_i(x_0, y_0)$ is the transmitted wave, $E_s(x_0, y_0)$ is the scattered wave from the object, and $O_r(x_0, y_0)$ and $O_t(x_0, y_0)$ are the coefficients of reflection and transmission, respectively. In the experiment, the SPD only collects the scattered wave [$E_s(x_0, y_0)$], which can be achieved by blocking the directly reflected/transmitted light in front of the detector, as shown in Figs. 4 and 5. Thus, after the light passes through the beam stop, the reflected wave or the transmitted wave is blocked such that $O_r(x_0, y_0) = O_t(x_0, y_0) = 0$. The light field amplitude distribution at the plane of the beam block can be expressed as follows:

$$E_B(x, y) = m(x, y) \cdot \iint E_s(x_0, y_0)$$
$$\times \exp\left\{\frac{ik}{2r}[(x - x_0)^2 + (y - y_0)^2]\right\} dx_0 dy_0, \quad (4)$$

where x and y are the spatial coordinates of the beam stop, r is the distance between the object and the beam stop, and $m(x, y)$ is the pupil function of the beam stop. When light is incident on an object, a portion of the light will scatter depending on the geometry of the object. For pure phase objects, as the phase gradient increases, scattering will also increase, which can be used to reveal the edge of the objects. Therefore, for dark-field GI, we can observe the edges by collecting the partially scattered light. The detected intensity I_{DF} can be expressed as follows:

$$I_{DF} = \iint \left\{ \iint E_B(x, y) \right.$$
$$\left. \times \exp\left\{\frac{ik}{2r'}[(x' - x)^2 + (y' - y)^2]\right\} dx dy \right\}^2 dx' dy', \quad (5)$$

where x' and y' are the spatial coordinates of the SPD, r' is the distance from the beam stop to the SPD, and $E_s(x, y)$ is the amplitude distribution of the scattered light after passing through the beam stop. The edge of the phase object can be considered as $O''(x_0, y_0)$, which indicates the alteration of the phase object $O(x_0, y_0)$. In the setup, the SPD is close to the beam stop. Thus, $I_{DF} \approx \iint |E_B(x, y)|^2 dx dy$. The edge of the phase object $O''(x_0, y_0)$ can be retrieved by the following equation:

$$O''(x_0, y_0) = \langle I_{DF} P(x_0, y_0) \rangle - \langle I_{DF} \rangle \langle P(x_0, y_0) \rangle. \quad (6)$$

Note that not all the scattered light can be collected by the SPD, as this depends on the sensitive area of the beam stop and the SPD. A smaller beam stop area can allow more scattered light to be collected but cannot be smaller than the cross-sectional area of the incident beam. Moreover, although a larger sensitive area of the detector allows for collecting more scattered light, it may increase the equipment cost. In Section 3.C we show that UV-CGI can detect the edges of pure phase objects and small scratches on a CD.

3. RESULTS AND DISCUSSION

A. Experimental Setup

The experimental setup of our UV-CGI system is shown in Fig. 1(a). A commercial 325 nm He–Cd laser (IK3301R-G,
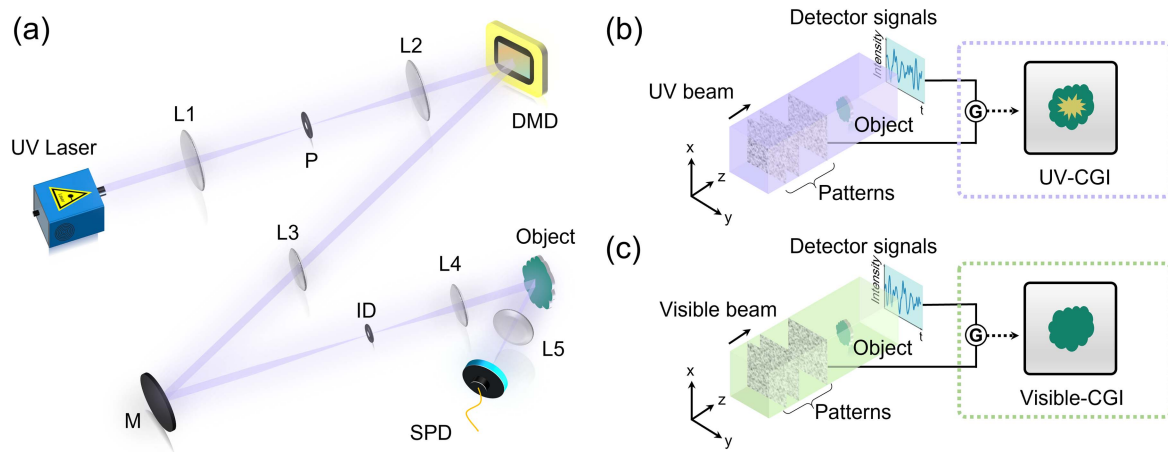
Fig. 1. Schematics of ultraviolet computational ghost imaging (UV-CGI). (a) Experimental setup. L1–L5, lenses; P, pinhole; DMD, digital micromirror device; M, mirror; ID, iris diaphragm; SPD, single-pixel detector. (b) UV-sensitive image of the object; the yellow part within the image represents the area that contains UV-sensitive samples. (c) As a comparison, traditional visible CGI cannot reveal such a UV image.

Kimmon Koha) is used as the light source. The laser beam is first expanded and spatially filtered by a 50 μm pinhole. Then the beam illuminates a high-speed DMD (GmbH V-7001, ViALUX), which generates a series of random modulation patterns at a refresh rate of 10.6 kHz. The patterns have a resolution of 64 × 64 superpixels (12 × 12 micromirrors per superpixel) extending over the central 768 × 768 pixels of the DMD. A 4f system consisting of two lenses (L3 and L4) is used to project these patterns onto the object plane. The resolution in each experiment can be calculated by $\Delta_r = N \cdot R \cdot M$, where N represents the number of pixels used on the DMD as a superpixel, $R = 13.7$ μm is the size of each DMD pixel, and $M = 2$ is the magnification of the modulation pattern on the object. An iris diaphragm (ID) is used to transmit only the zero-order diffraction beam. A collection lens focuses the backscattered light from the sample onto a photodiode SPD (PDAPC2, Thorlabs), which has a spectral response from 320 to 1100 nm. A data acquisition module (USB-6353, National Instruments) synchronizes the DMD and SPD. Samples sensitive to UV light but not visible to the naked eye were chosen as objects. By correlating the illuminating patterns and measured light intensities, the UV-CGI images can be reconstructed by various algorithms, as portrayed in the yellow area of Fig. 1(b), whereas with visible light no image can be seen, as shown in Fig. 1(c). Here, we use the alternating projection algorithm to reconstruct the images [48].

B. Demonstration of UV-CGI with UV-Sensitive Samples

We first used chemical sunscreen, which can absorb UV light, as the sample. Three different samples were prepared, as shown in the left columns of Figs. 2(a)–2(c). The first was a sponge (38 mm × 32 mm) coated with sunscreen, except for a triangular area in the center. The second one (25 mm × 18 mm) was similar to the first but had an umbrella-shaped uncoated area with a visible "UV" written on it. The area without sunscreen forms an umbrella, as shown in Fig. 2(b). The third sample was a triangular piece of paper supported on a thin wire; a small area
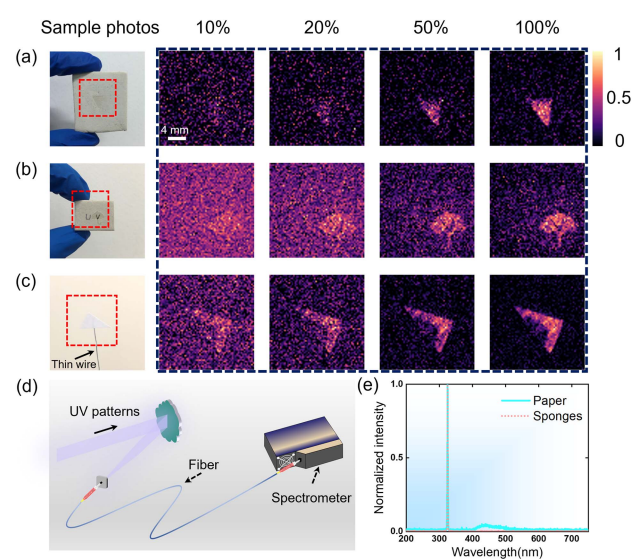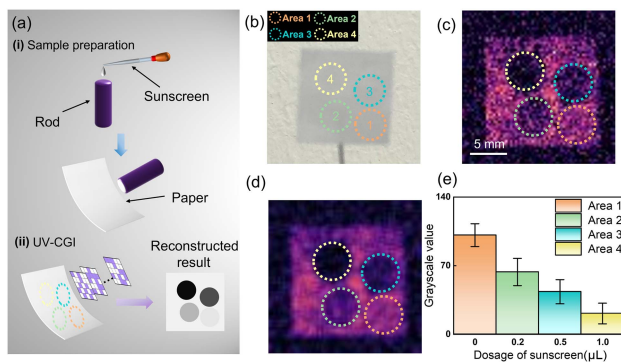

Fig. 2. Reconstructed images of three different samples for sampling ratios of 10%, 20%, 50%, and 100%. The left columns show the ground-truth photos of the samples: (a) sponge coated with sunscreen except in the central triangular area; (b) sponge coated with sunscreen except in an umbrella-shaped area with the letters "UV" written on it; (c) bottom part of a triangular piece of paper coated with sunscreen. (d) Schematic diagram of the spectral measurement. (e) Measurement spectra of the paper and the sponges under UV irradiation.

near the hypotenuse of the triangle was coated with sunscreen. The reconstructed images (64 × 64 resolution) of these samples, under different sampling rates, are shown within the black dashed box of Figs. 2(a)–2(c). The shapes of the uncoated areas, which cannot be observed clearly by visible photography, emerge with improved clarity as the sampling ratio increases from 10% to 100% under UV-CGI. For the first two samples, the triangular and umbrella areas become apparent starting from a sampling ratio of 50%, while the basic shape of the third

sample appears at a sampling ratio of 10%. In the second sample the "UV" letters can be seen clearly under visible photography, but the UV-CGI reconstructed image only reveals the shape of the umbrella area, showing the difference between visible and UV photography. For the third sample, the area coated with sunscreen cannot be observed under visible light, as shown in the left column of Fig. 2(c). However, a dark area near the hypotenuse of the triangle is shown clearly in the reconstructed UV images. These results prove that UV-CGI can be used to detect the areas that contain UV-sensitive matter. It should be noted that the reconstructed images of the third sample have better quality than those of the other two samples, especially at a sampling rate of 10%. This is because the third sample has almost no background noise, while the other two suffer from spurious reflection from the area coated with sunscreen. We further measured the spectra of these samples under UV light irradiation, as shown in Fig. 2(d). It can be seen in Fig. 2(e) that all the samples have peaks at 325 nm. However, the sponges barely respond at other wavelengths, showing only a UV spectral line. A small peak is displayed at 400–500 nm for the paper, indicating that the SPD has also collected the visible fluorescence induced by the fluorescent powder in the paper. This is another reason why the reconstructed images of the third sample have better quality than those of the other two samples.

We further demonstrate that UV-CGI can be used to detect UV-sensitive samples with different densities, which are the ratio between the sample volume and the distribution area. We prepared a sample consisting of four circular areas containing different densities of sunscreen. Figure 3(a) shows a schematic of the sample preparation. We first use a small rod to imprint given volumes/doses of sunscreen onto a square piece of paper. A photograph of the sample is shown in Fig. 3(b), in which the differently colored dotted circles indicate the four areas stamped, respectively, with volumes of 0, 0.2, 0.5, and 1.0 µL. It is not easy to distinguish the different densities with the naked eye. Figure 3(c) shows the reconstructed UV-CGI images (64×64 resolution) of these four areas from 8192 sampling frames. Different grayscale values are shown for each

area, corresponding to different densities of the sunscreen. A 3×3 kernel is used to smooth the image, as shown in Fig. 3(d). To measure the densities of the sunscreen in the four areas, we calculate the standard deviation of the grayscale values, as shown in Fig. 3(e). The statistical results are, respectively, 101.2 ± 11.6, 63.6 ± 13.9, 43.4 ± 12.3, and 21.2 ± 10.6. It can be seen that the higher the sunscreen density, the lower the grayscale value. This is because sunscreen absorbs UV light, which decreases the reflected UV light collected by the detector.
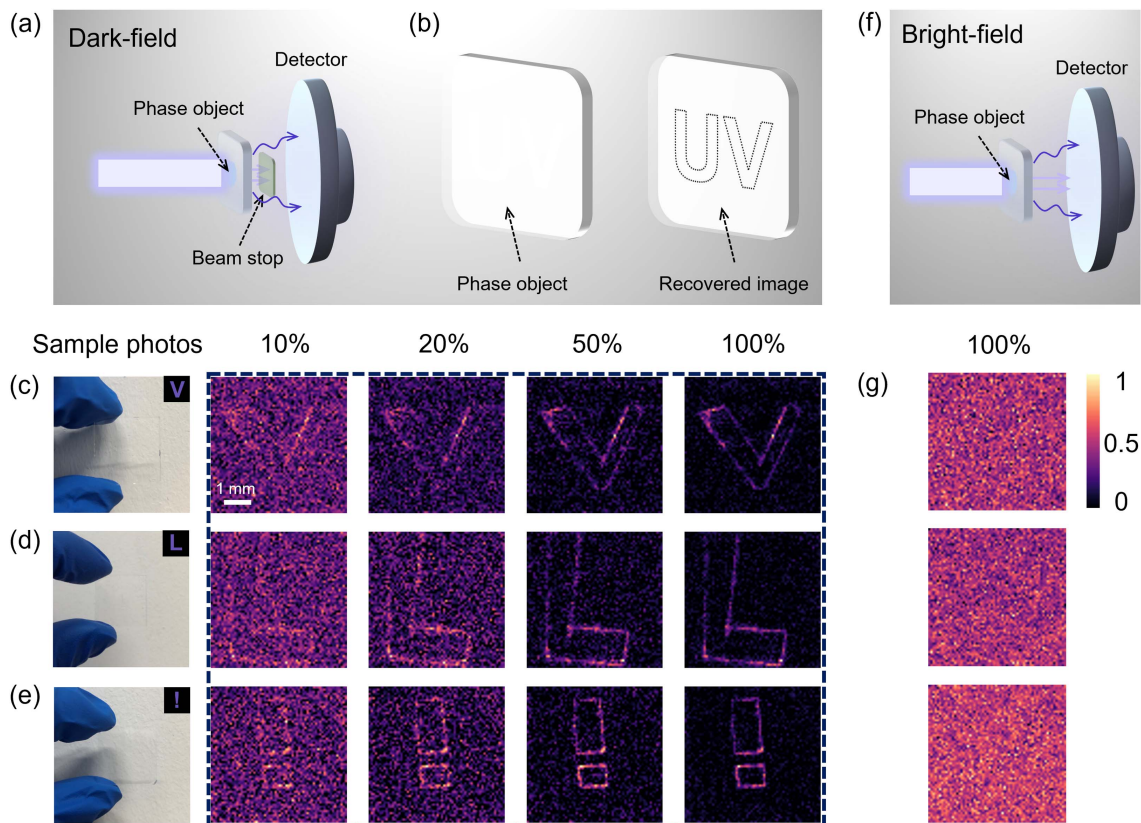
C. Dark-Field UV-CGI to Detect Phase Objects and Small Defects

Due to its shorter wavelength, UV reflectance photography has the advantages of detecting fine scratches and defects on metal and semiconductor surfaces, since short wavelength light is more strongly scattered [47]. On another note, dark-field imaging or detection is another powerful technique to enhance the contrast of transparent or translucent samples that are not imaged well under bright-field illumination [49]. Instead of collecting the directly transmitted light, dark-field imaging only collects the scattered light from samples, preventing the directly illuminated light from entering the detector. Therefore, it is suitable for revealing sample edges and refractive index gradients, for the characterization of nanomaterials through measuring the scattering spectra of individual nanoparticles, and for monitoring dynamic reactions at the single particle level, and so on.

In this section, we demonstrate a dark-field scheme for UV-CGI to detect the edges of phase objects and small scratches on a CD. The images are reconstructed by calculating the correlation between the intensity values of the scattered field and the DMD patterns.

1. Dark-Field UV-CGI with Pure Phase Objects

The high-contrast edge images of pure phase objects obtained with dark-field UV-CGI are shown in Fig. 4(a). The UV beam, after modulation by the DMD, illuminates the object and then the scattered light is collected by the SPD. A beam stop is placed behind the object to block the directly transmitted light. Figure 4(b) is a schematic diagram of a pure phase object, the edges of which can be revealed after using dark-field UV-CGI. The DMD memory buffer was initially loaded with 4096 random patterns with a resolution of 64×64, using 192×192 DMD pixels. One pixel of the illumination patterns was corresponding to about 82 µm on the object plane. The beam stop is 5.5 mm × 5.5 mm in size, large enough to block all the directly transmitted light. The object was placed just in front about 2 mm from the SPD. Three samples were made from scotch tape and pasted onto a silica substrate. The left column of Figs. 4(c)–4(e) shows the photos of the three samples: the letters 'V' and 'L', and an exclamation mark '!'. They cannot be seen clearly due to the almost complete transparency of these phase objects. The images were reconstructed with sampling ratios of 10%, 20%, 50%, and 100%, as shown in the black dashed box of Fig. 4. The edges of the three samples begin to appear in the image at a sampling ratio of 10%, and become quite clear at a sampling ratio of 50%. The inner part within the edges of the sample is invisible because almost

Fig. 3. Detection of sunscreen by UV-CGI. (a) Experimental procedure. (i) Sample preparation. (ii) UV-CGI exposures. (b) Visible light photos of the sample; the different colors indicate the four areas of the sample coated with different densities of sunscreen, areas 1–4 containing, respectively, 0, 0.2, 0.5, and 1 µL. (c) Reconstructed image of the sample, in which the four areas are shown with different grayscale values. (d) The smoothed result of (c). (e) Statistical grayscale values of the four areas in (d).

Fig. 4. Dark-field UV-CGI of transmissive pure phase objects (left side) and a comparison experiment in a bright-field (right side). (a) Experimental setup of transmissive dark-field UV-CGI. (b) Schematic of phase object and the recovered CGI image. (c)–(e) Reconstructed dark-field images of three samples for sampling ratios of 10%, 20%, 50%, and 100%. The left column shows the photos of two fingers holding the phase objects, which are the letters (c) "V", (d) "L", and (e) an exclamation mark "!". (f) Experimental setup of bright-field UV-CGI. (g) Reconstructed bright-field images of three samples for 100% sampling ratio.

no light is scattered there. As a comparison, the experimental results of bright-field UV-CGI are shown in Figs. 4(f) and 4(g); the former shows the experimental setup, and the latter the reconstructed images of the three samples. We can see that in the three images of Fig. 4(g), corresponding to the letters V, L, and "!", it is difficult to discern the edges of the objects, which are drowned in the noise.

2. Detecting Damage on a CD
Figure 5 illustrates the detection of small scratches on a CD by reflective dark-field UV-CGI. Figure 5(a) shows the experimental setup; the directly reflected light from the sample is blocked by the beam stop, so the SPD only collects part of the back-scattered light from the object. As shown in Fig. 5(b), there are two obvious defects (in the black dashed boxes) and three small scratches on the CD, which are a point-like scratch inside the red dashed box (1), a scratch inside the green box (2), and two scratches in the orange box (3), respectively. An enlargement of the minor defects is shown in the left column photos of Figs. 5(c)–5(e). The DMD patterns are the same as above. The reconstructed images are enclosed in the black dashed box of Figs. 5(c)–5(e). It can be seen that the image of the point-like scratch is already visible at the sampling rate of 10%, and is more apparent than the other two line-scratches [Figs. 5(d) and 5(e)]. This is because it is composed of multiple

small scratches with more unevenness on the surface, so it scatters more light. The reconstructed image in Fig. 5(c) has relatively high contrast at a sampling rate of 50%, almost the same as that at a sampling rate of 100%. However, in Figs. 5(d) and 5(e), the scratches are relatively shallow so scattering is not so strong and the reconstructed images at a sampling rate of 20% have a highly noisy background. The image quality and contrast improve when the sampling rate increases to 50% and 100%, especially for the pair of line scratches in Fig. 5(e). As a comparison, the results of bright-field UV-CGI are shown on the right side of Fig. 5, where Fig. 5(f) is a schematic of the experimental setup. Figure 5(g) shows the reconstructed images of the three damaged areas on the CD; here we cannot see the blemishes, since the scattered light from the scratches is too weak and is buried in the directly reflected light.

4. CONCLUSION

In summary, we have experimentally demonstrated UV-CGI using random spatial modulation patterns and an SPD. Through a comparison of different densities of UV-sensitive sunscreen samples, different grayscale values were obtained for the reconstructed images, representing different sample densities. We have also demonstrated a dark-field UV-CGI method to detect phase objects, by collecting only the scattered
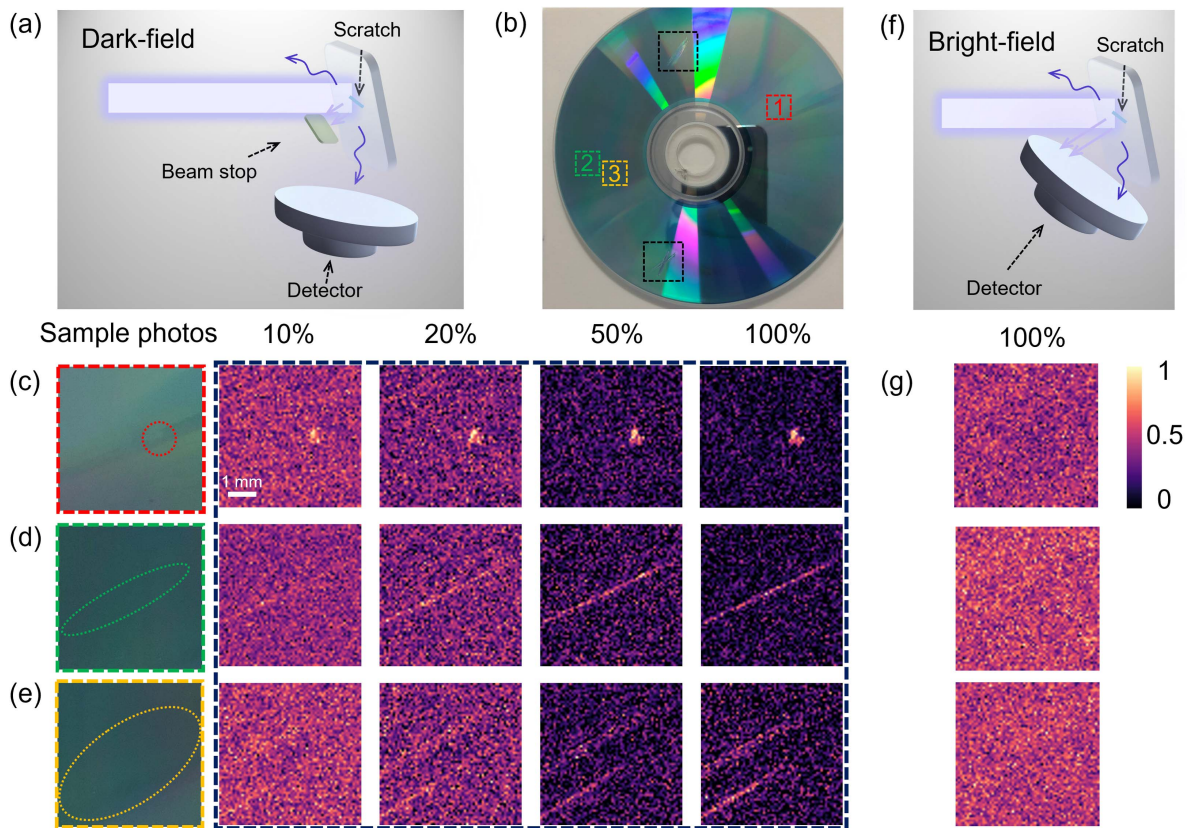
Fig. 5. Detection of the damages on a CD by dark-field UV-CGI (left side) and a comparative experiment in a bright-field UV-CGI (right side). (a) Experimental setup of reflective dark-field UV-CGI. (b) Photograph of the damaged CD. Three slightly damaged areas are shown in the colored boxes, corresponding to (1) a point-like scratch, (2) a line scratch, and (3) two line scratches. Another two heavily damaged areas are indicated by the black boxes as a comparison. (c)–(e) Reconstructed dark-field images of areas (1)–(3) in (b) for sampling ratios of 10%, 20%, 50%, and 100%. The left column shows the magnified photos of the three areas. (f) Experimental setup of bright-field UV-CGI. (g) Reconstructed bright-field images of the three areas for 100% sampling ratios.

light from the edges. Due to the short wavelength of UV light, high-contrast images of the fine defects on a CD can be reconstructed, with the capability to resolve ∼82 μm.

Further modifications of UV-CGI can be studied to improve its performance. For example, the system can be optimized with custom designed coded masks or diffusers as the SLM [17,24,25] to increase imaging speed and reduce system size. Versatile imaging techniques, such as multispectral and time-resolved imaging [50], can also be introduced for UV-CGI in nondestructive testing, component analysis, or biological fluorescence imaging. Machine-learning algorithms can also help improve imaging speed and the resulting image quality [51]. Our scheme provides a cost-effective UV imaging and detection solution that can open up new opportunities and applications for computational imaging in the UV band.

APPENDIX A: INFLUENCE OF THE BEAM STOP'S SIZE, LOCATION, AND SHAPE

We further studied the influence of the beam stop's size, location, and shape in transmissive dark-field UV-CGI, as shown in Fig. 6. Here we used a transparent square phase object of size 3.5 mm × 3.5 mm [Fig. 6(a)]. The object was placed in the center of the illumination beam. We considered five different

cases of the beam stops, as shown in Figs. 6(b)–6(f). For the first four cases, we used a square-like beam stop, similar to the shape of the illumination beam, but with different arrangements. (1) Fig. 6(b), the size of the beam stop (about 3.7 mm × 3.7 mm) is slightly larger than that of the illumination beam; (2) Fig. 6(c), the size of the beam stop (about 8.0 mm × 8.0 mm) is much larger than that of the illumination beam; (3) Fig. 6(d), the same large beam stop as used in case (2), but with its upper right corner aligned with the light beam; (4) Fig. 6(e), similar to case (3), but with its lower left corner aligned with the light beam. For case (5), Fig. 6(f), a circular beam stop of diameter 5.3 mm is used for another comparison.

The reconstructed dark-field images with a sampling rate of 100% are presented in Figs. 6(g)–6(k), corresponding to the beam stops used in Fig. 6(b)–6(f). The reconstructed image of case (1) in Figs. 6(b) and 6(g) has the best image quality among the five cases. This is because the setup in this case can not only collect the most scattered light but also block all the directly transmitted light. The reconstructed image of case (2) in Figs. 6(c) and 6(h) does not show any edges of the object, since the setup in this case blocks most of the scattered light. For cases (3) and (4), most parts of the object edges can be reconstructed. However, both of the edges located at the
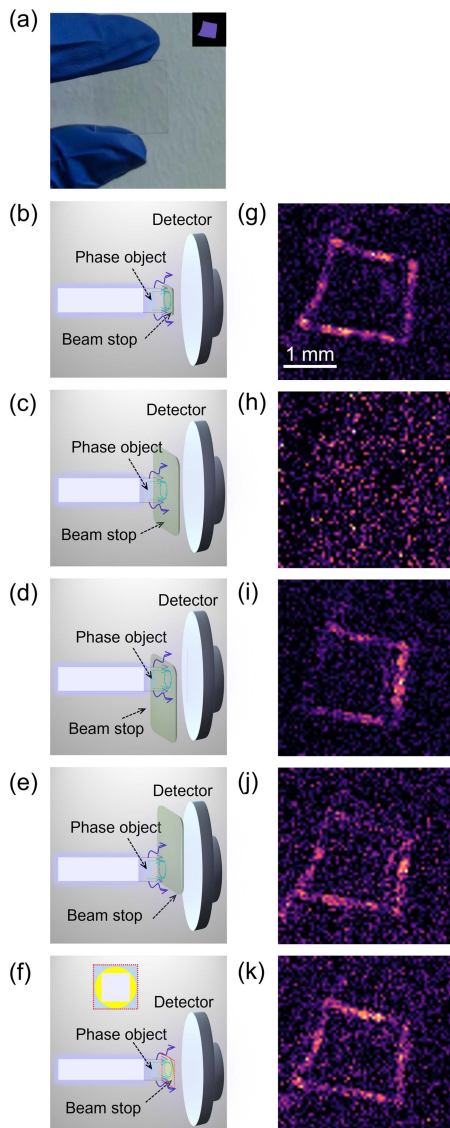
Fig. 6. Dark-field UV-CGI with different kinds of beam stops in the transmission scheme. (a) Photo of the transparent square phase object, of size 3.5 mm × 3.5 mm; its shape is shown in the upper right corner. The five different beam stops are shown in (b)–(f). (b) The beam stop has a size (about 3.7 mm × 3.7 mm) approximately equal to the object's size. (c) The beam stop has a size (about 8.0 mm × 8.0 mm) that is larger than object's size. (d) Same large beam stop used in (c) but moved such that the beam passes through its upper right corner. (e) Similar to (d), but with the beam passing through the lower left corner. (f) Circular beam stop of diameter 5.3 mm, as indicated by the yellow circular area in the inset; the square inside the yellow circle indicates the illumination beam, which encompasses the phase object. The reconstructed results corresponding to the cases (b)–(f) are shown in (g)–(k), with a sampling rate of 100%.

lower left corner in Fig. 6(i) and upper right corner in Fig. 6(j) cannot be well reconstructed because the scattered light corresponding to these parts is blocked by the misaligned beam stop. For case (5) in Figs. 6(f) and 6(k), the shape of the phase object has been reconstructed but has more noise compared with case

(1) in Figs. 6(b) and 6(g) since the circular beam stop in case (5) also blocks a small part of the scattered light, although all the directly transmitted light is rejected by the setup. A smaller beam stop would allow parts of the directly transmitted light to be collected by the detector, which would lead to poor image quality.

We can conclude that a suitable beam stop in dark-field UV-CGI should have a size that is equal to or slightly larger than the illumination beam to block all the directly transmitted light, and also allow the detector to collect as much scattered light as possible from the object. The beam stop should also have a similar shape to the illumination beam; otherwise the reduced scattered light collected by the detector would lead to reduced image quality. The beam stop should also block all the directly transmitted light to avoid the weak scattered light being buried in the directly transmitted light. We note that similar conclusions in this part are also applicable to the scheme of dark-field reflective UV-CGI.

APPENDIX B: ANALYSIS OF IMAGE QUALITY AT DIFFERENT SAMPLING RATIOS IN SIMULATION RESULTS

To evaluate the image quality at different sampling ratios in dark-field UV-CGI, we conduct simulations to detect the edges of a pure phase object as well as a comparison study in the bright-field condition, as shown in Fig. 7. The amplitude and phase of the original object are shown in Fig. 7(a). By comparing the reconstructed images with the edge area of the original phase, we evaluate the reconstructed results by the mean square error (MSE) and the peak signal to noise ratio (PSNR) in Fig. 7(b), with sampling rates ranging from 5% to 100%. The results show that the PSNR increases from 5.9 to 8.17 dB and the MSE decreases from 0.25 to 0.15, respectively, indicating that the image quality improves with increasing sampling rate. Examples of the reconstructed dark-field images are shown
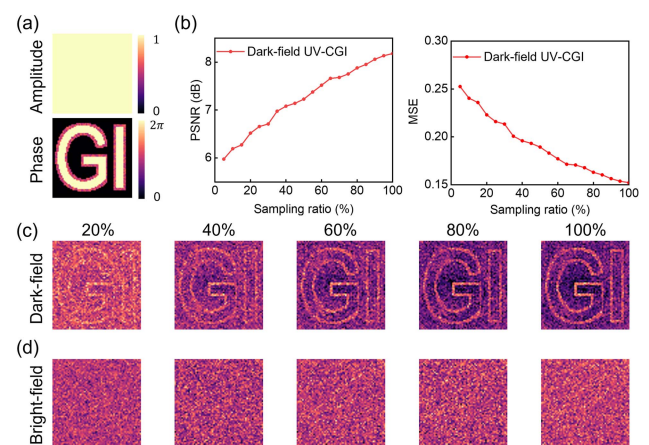
Fig. 7. Simulation results of dark-field UV-CGI with a pure phase object and comparison results in the bright-field condition. (a) Amplitude (upper) and phase (lower) of the original object. (b) PSNR and MSE curves of the reconstructed dark-field edge images versus sampling ratio, from 5% to 100%. (c) Example of reconstructed dark-field images with different sampling ratios. (d) Reconstructed bright-field images with the same sampling ratios as in (c).

in Fig. 7(c), where the sampling ratio increases from 20% to 100%. The dark-field UV-CGI can reconstruct a blurry edge even under a sampling ratio of 20%. As the sampling rate increases, the edges of the phase object become clearer and clearer. Figure 7(d) shows the reconstructed bright-field images with the same sampling ratios as in Fig. 7(c). None of the edges of the phase object can be reconstructed by the bright-field UV-CGI.

Disclosures. The authors declare no conflicts of interest.

Data Availability. The data that support the findings of this study are available from the corresponding author upon reasonable request.

REFERENCES

1. T. B. Pittman, Y. H. Shih, D. V. Strekalov, _et al._, "Optical imaging by means of two-photon quantum entanglement," Phys. Rev. A **52**, R3429–R3432 (1995).
2. M. J. Padgett and R. W. Boyd, "An introduction to ghost imaging: quantum and classical," Philos. Mag. A **375**, 20160233 (2017).
3. D. Zhang, Y.-H. Zhai, and L.-A. Wu, "Correlated two-photon imaging with true thermal light," Opt. Lett. **30**, 2354–2356 (2005).
4. J. H. Shapiro, "Computational ghost imaging," Phys. Rev. A **78**, 061802 (2008).
5. Y. Bromberg, O. Katz, and Y. Silberberg, "Ghost imaging with a single detector," Phys. Rev. A **79**, 053840 (2009).
6. M. F. Duarte, M. A. Davenport, D. Takhar, _et al._, "Single-pixel imaging via compressive sampling," IEEE Signal Process Mag. **25**, 83–91 (2008).
7. M. P. Edgar, G. M. Gibson, and M. J. Padgett, "Principles and prospects for single-pixel imaging," Nat. Photonics **13**, 13–20 (2018).
8. G. M. Gibson, S. D. Johnson, and M. J. Padgett, "Single-pixel imaging 12 years on: a review," Opt. Express **28**, 28190–28208 (2020).
9. C. Zhao, W. Gong, M. Chen, _et al._, "Ghost imaging lidar via sparsity constraints," Appl. Phys. Lett. **101**, 141123 (2012).
10. M. J. Sun, M. P. Edgar, G. M. Gibson, _et al._, "Single-pixel three-dimensional imaging with time-based depth resolution," Nat. Commun. **7**, 12010 (2016).
11. S. Ota, R. Horisaki, Y. Kawamura, _et al._, "Ghost cytometry," Science **360**, 1246–1251 (2018).
12. L. Olivieri, J. S. T. Gongora, L. Peters, _et al._, "Hyperspectral terahertz microscopy via nonlinear ghost imaging," Optica **7**, 186 (2020).
13. Y. Qi, Z. H. Lim, L. Li, _et al._, "Hadamard transform-based hyperspectral imaging using a single-pixel detector," Opt. Express **28**, 16126–16139 (2020).
14. S. Jin, W. Hui, Y. Wang, _et al._, "Hyperspectral imaging using the single-pixel Fourier transform technique," Sci. Rep. **7**, 45209 (2017).
15. Y. Liu, J. Suo, Y. Zhang, _et al._, "Single-pixel phase and fluorescence microscope," Opt. Express **26**, 32451–32462 (2018).
16. Y.-N. Zhao, H.-Y. Hou, J.-C. Han, _et al._, "Single-pixel phase microscopy without 4f system," Opt. Lasers Eng. **163**, 107474 (2023).
17. X.-H. Chen, Q. Liu, K.-H. Luo, _et al._, "Lensless ghost imaging with true thermal light," Opt. Lett. **34**, 695–697 (2009).
18. B. Liu, F. Wang, C. Chen, _et al._, "Single-pixel diffuser camera," IEEE Photon. J. **13**, 7800205 (2021).
19. L. Y. Dou, D. Z. Cao, L. Gao, _et al._, "Dark-field ghost imaging," Opt. Express **28**, 37167–37176 (2020).
20. W. Li, X. Hu, J. Wu, _et al._, "Dual-color terahertz spatial light modulator for single-pixel imaging," Light Sci. Appl. **11**, 191 (2022).
21. B. Liu, F. Wang, C. Chen, _et al._, "Self-evolving ghost imaging," Optica **8**, 1340–1349 (2021).
22. D. Wang, B. Liu, J. Song, _et al._, "Dual-mode adaptive-SVD ghost imaging," Opt. Express **31**, 14225–14239 (2023).
23. W. Jiang, Y. Yin, J. Jiao, _et al._, "2,000,000 fps 2D and 3D imaging of periodic or reproducible scenes with single-pixel detectors," Photon. Res. **10**, 2157–2164 (2022).
24. E. Hahamovich, S. Monin, Y. Hazan, _et al._, "Single pixel imaging at megahertz switching rates via cyclic Hadamard masks," Nat. Commun. **12**, 4516 (2021).
25. W. Jiang, J. Jiao, Y. Guo, _et al._, "Single-pixel camera based on a spinning mask," Opt. Lett. **46**, 4859–4862 (2021).
26. N. Bornman, M. Agnew, F. Zhu, _et al._, "Ghost imaging using entanglement-swapped photons," npj Quantum Inf. **5**, 63 (2019).
27. Z. Ye, H. Wang, J. Xiong, _et al._, "Simultaneous full-color single-pixel imaging and visible watermarking using Hadamard-Bayer illumination patterns," Opt. Laser Eng. **127**, 105955 (2020).
28. G. Wang, H. Zheng, Z. Tang, _et al._, "All-optical naked-eye ghost imaging," Sci. Rep. **10**, 2493 (2020).
29. G. M. Gibson, B. Sun, M. P. Edgar, _et al._, "Real-time imaging of methane gas leaks using a single-pixel camera," Opt. Express **25**, 2998–3005 (2017).
30. Y. Wang, K. Huang, J. Fang, _et al._, "Mid-infrared single-pixel imaging at the single-photon level," Nat. Commun. **14**, 1073 (2023).
31. C. M. Watts, D. Shrekenhamer, J. Montoya, _et al._, "Terahertz compressive imaging with metamaterial spatial light modulators," Nat. Photonics **8**, 605–609 (2014).
32. R. I. Stantchev, D. B. Phillips, P. Hobson, _et al._, "Compressed sensing with near-field THz radiation," Optica **4**, 989–992 (2017).
33. D. Pelliccia, A. Rack, M. Scheel, _et al._, "Experimental X-ray ghost imaging," Phys. Rev. Lett. **117**, 113902 (2016).
34. A.-X. Zhang, Y.-H. He, L.-A. Wu, _et al._, "Tabletop X-ray ghost imaging with ultra-low radiation," Optica **5**, 374–377 (2018).
35. H. Yu, R. Lu, S. Han, _et al._, "Fourier-transform ghost imaging with hard X rays," Phys. Rev. Lett. **117**, 113901 (2016).
36. Y.-H. He, A.-X. Zhang, M.-F. Li, _et al._, "High-resolution sub-sampling incoherent X-ray imaging with a single-pixel detector," APL Photon. **5**, 056102 (2020).
37. R. I. Khakimov, B. M. Henson, D. K. Shin, _et al._, "Ghost imaging with atoms," Nature **540**, 100–103 (2016).
38. S. Li, F. Cropp, K. Kabra, _et al._, "Electron ghost imaging," Phys. Rev. Lett. **121**, 114801 (2018).
39. A. M. Kingston, G. R. Myers, D. Pelliccia, _et al._, "Neutron ghost imaging," Phys. Rev. A **101**, 053844 (2020).
40. Y. H. He, Y. Y. Huang, Z. R. Zeng, _et al._, "Single-pixel imaging with neutrons," Sci. Bull. **66**, 133–138 (2021).
41. J. Zhang, Q. Wang, J. Dai, _et al._, "Demonstration of a cost-effective single-pixel UV camera for flame chemiluminescence imaging," Appl. Opt. **58**, 5248–5256 (2019).
42. J.-T. Ye, C. Yu, W. Li, _et al._, "Ultraviolet photon-counting single-pixel imaging," Appl. Phys. Lett. **123**, 024005 (2023).
43. Q. Zhuang, Y. Peng, D. Yang, _et al._, "UV-fluorescence imaging for real-time non-destructive monitoring of pork freshness," Food Chem **396**, 133673 (2022).
44. R. S. P. King, L. W. L. Davis, and D. A. Skros, "The use of longwave reflected UV imaging for the enhancement of cyanoacrylate developed fingermarks: a simple, safe and effective imaging tool," Forensic Sci. Int. **289**, 329–336 (2018).
45. K. K. Patel, A. Kar, and M. A. Khan, "Potential of reflected UV imaging technique for detection of defects on the surface area of mango," Food Sci. Technol. Res. **56**, 1295–1301 (2019).
46. G. A. Shaw, A. M. Siegel, J. Model, _et al._, "Deep UV photon-counting detectors and applications," Proc. SPIE **7320**, 73200J (2009).
47. Z. Ren, F. Fang, N. Yan, _et al._, "State of the art in defect detection based on machine vision," Int. J. Precis. Eng. Manuf. Green Technol. **9**, 661–691 (2021).

48. K. Guo, S. Jiang, and G. Zheng, "Multilayer fluorescence imaging on a single-pixel detector," Biomed. Opt. Express **7**, 2425–2431 (2016).
49. P. F. Gao, G. Lei, and C. Z. Huang, "Dark-field microscopy: recent advances in accurate analysis and emerging applications," Anal. Chem. **93**, 4707–4726 (2021).
50. F. Rousset, N. Ducros, F. Peyrin, *et al.*, "Time-resolved multispectral imaging based on an adaptive single-pixel camera," Opt. Express **26**, 10550–10558 (2018).
51. Y. He, G. Wang, G. Dong, *et al.*, "Ghost imaging based on deep learning," Sci. Rep. **8**, 6469 (2018).